Photoelectrochemical imaging system with high spatiotemporal resolution for visualizing dynamic cellular responses

Bo Zhou[1], Anirban Das[1,*], Muchun Zhong[1], Qian Guo[1], De-Wen Zhang[2], Karin A. Hing[1], Ana Jorge Sobrido[1], Maria-Magdalena Titirici[3], Steffi Krause[1,*]

[1]School of Engineering and Materials Science, Queen Mary University of London, Mile End Road, London E1 4NS, UK

[2]Institute of Medical Engineering, School of Basic Medical Sciences, Health Science Center, Xi'an Jiaotong University, Xi'an, 710061, China

[3]Department of Chemical Engineering, Imperial College London, South Kensington Campus, SW7 2AZ

s.krause@qmul.ac.uk, anirbanscon@gmail.com

Abstract

Photoelectrochemical imaging has great potential in the label-free investigation of cellular processes. Herein, we report a new fast photoelectrochemical imaging system (PEIS) for DC photocurrent imaging of live cells, which combines high speed with excellent lateral resolution and high photocurrent stability, which are all crucial for studying dynamic cellular processes. An analog micromirror was adopted to raster the sensor substrate, enabling high-speed imaging. α-Fe_2O_3 (hematite) thin films synthesized via electrodeposition were used as a robust substrate with high photocurrent and spatial resolution. The capabilities of this system were demonstrated by monitoring cell responses to permeabilization with Triton X-100. The ability to carry out dynamic functional imaging of multiple cells simultaneously provides improved confidence in the data than could be achieved with the slower electrochemical single-cell imaging techniques described previously. When

monitoring pH changes, the PEIS can achieve frame rates of 8 frames per second.

Keywords

Real-time cell imaging, fast high-resolution electrochemical imaging, light-activated electrochemistry, light-addressable potentiometric sensors, hematite electrode

1. Introduction

Today's life science research is increasingly focusing on the understanding of complex and fast dynamic cellular processes and cellular responses to external stimuli in real time. Several 'live-cell imaging' techniques have evolved to partially address these challenging demands enabling interrogation of dynamic cellular processes over both spatial and temporal scales in contrast to fixed-cell imaging where cellular activity is frozen to a single point in time (Decelle et al. 2020; Stephens and Allan 2003). However, the commonly adopted fluorescent based microscopic techniques can suffer from photobleaching over time and can require use of fluorescent tags that may significantly alter the biological activity of small biomolecules (Giepmans et al. 2006). These limitations are mitigated by label-free electrochemical imaging such as plasmonic-based electrochemical impedance microscopy (P-EIM), which has been used for imaging cell impedance (Wang et al. 2011) and action potentials (Liu et al. 2017) and electroanalytical scanning probe techniques such as scanning electrochemical microscopy (SECM) (Bard et al. 1989; Sun et al. 2007) and scanning ion conductance microscopy (SICM) (Chen et al. 2012; Hansma et al. 1989). SECM is capable of imaging substrate topography and local reactivity with high spatial resolution (Polcari et al. 2016) and has been used for the study of membrane proteins (Arai et al. 2013) and cellular responses (Bergner et al. 2011).

SICM allows high-resolution topographic imaging of live cells (Chen et al. 2012) and the imaging of cell surface charges (Perry et al. 2016). However, the imaging speeds of scanning probe techniques are limited making it difficult to image the responses of multiple cells simultaneously and in real time. Considering the challenge arising from the extreme mechanical compliance and susceptibility of living cells to external stimuli induced by mechanical or optical probing, light-addressable electrochemical techniques may be ideally suited to observe living cells with minimal invasiveness.

2-D Photoelectrochemical imaging evolved primarily with light-addressable potentiometric sensors (LAPS) (Hafeman et al. 1988; Wu et al. 2017a) where a flat, featureless electrolyte-insulator-semiconductor field-effect structure under an applied bias is addressed by a modulated focused light beam thereby exciting a local alternating current (AC) photocurrent without any complicated electrical wiring or microelectrode probing. In LAPS, the charged species adjacent to the insulator surface affect the width of the space charge region and hence the magnitude and phase of the AC current. Thus, by monitoring the photocurrent generated at the point of illumination, LAPS can visualize local ion concentrations (Das et al. 2013; Das et al. 2015; Yoshinobu et al. 2005) and acidification by cells such as *Escherichia coli* (Yoshinobu et al. 1997). Extended functionality can be achieved with light-activated electrochemistry (LAE) where an electrolyte-semiconductor structure is used to perform faradaic electrochemistry locally at the site of illumination (Choudhury et al. 2015; Parker et al. 2018; Zarei et al. 2018). Recently, we have shown that an AC photoelectrochemical imaging system (PEIS) based on LAE with indium tin oxide (ITO) substrates (Wu et al. 2019) can successfully image the surface charge of isolated living cells with subcellular resolution. When the ITO electrode is biased towards depletion and under supra-bandgap illumination, photogenerated minority carriers (holes) move towards the electrode/electrolyte interface where the oxidation of hydroxide ions to hydroxyl radicals takes place resulting in a photocurrent, which is lower under cells

due to a blocked diffusion of the electroactive species caused by cell surface charge and the narrow gap between the cell and the ITO surface. Despite the potential of LAPS and LAE in electrochemical imaging, the uptake of this technology for visualizing dynamic physiological events is restricted due to limitations in the speed or resolution of existing imaging systems. High-resolution LAPS and LAE technologies suffer from relatively slow imaging speed as the scans are commonly performed using the mechanical movement of the sample mounted on an XYZ positioning system, while the high-speed imaging systems developed for LAPS to date show poor spatial resolution (Das et al. 2014a; Das et al. 2014b; Miyamoto et al. 2014; Yoshinobu et al. 2017).

Another important factor in the performance of LAPS and LAE systems is the choice of semiconductor substrate. While silicon clearly outperforms other semiconductors in LAPS - submicron resolution was achieved using a silicon-on-sapphire substrate (Wang et al. 2015) - LAE with silicon requires modification of the semiconductor with a self-assembled organic monolayer (Vogel et al. 2019). A number of alternative semiconductor substrate materials that can be used for LAE without further modification have been tested with regards to their biocompatibility, stability and performance. ITO was used successfully for live cell imaging with LAE with good lateral resolution (Wu et al. 2019), but suffers from poor photocurrent stability, low photocurrents and a high photocurrent onset potential, which affects the signal-to-noise ratio and increases the risk of damaging cells on the electrode surface. Due to the low minority charge carrier mobility in ITO, the maximum light-modulation frequency that could be employed was 10 Hz resulting in slow scanning speeds. Higher modulation frequencies, higher photocurrents and a lower photocurrent onset potential were achieved with InGaN (Zhou et al. 2019), however the photocurrent stability was not sufficient for bioimaging applications. Hematite is a promising substrate that has been used to detect NADH (reduced form of nicotinamide adenine dinucleotide) photoelectrochemically under visible light

irradiation (Ryu et al. 2015), and was also reported as LAE substrate to detect dopamine with good reproducibility, showing a potential for chemical imaging (Seo et al. 2018). Hematite has a narrow bandgap (1.9 eV~2.2 eV) (Phuan et al. 2017; Tamirat et al. 2016), which allows a range of wavelengths in the visible range to be employed for photocurrent excitation. Based on its short minority carrier diffusion length of 2-4 nm (Bohn et al. 2012; Kennedy 1978), high spatial resolution imaging should be possible with this material. Notably, hematite has a good chemical stability, especially high resistance to photocorrosion due to its very slow decomposition reaction kinetics (Jiang et al. 2017). Moreover, non-toxicity, low cost, ease of synthesis and earth-abundance make it attractive as sensor material for live cell applications.

In the current work, we report a PEIS with fast scanning capability that works for both, LAPS or LAE, and can visualize dynamic cellular events with micron resolution. A significant increase in the scanning speed was achieved through use of a micro-mirror to move the laser spot, in contrast to slower high-resolution setups where the sample holder was moved with respect to the laser beam with a mechanical positioning system.

2. Materials and methods

2.1. Instrumentation

The experimental setup that has been used for AC and DC photocurrent imaging is shown in Figure 1. A laser diode module (BioRay™ Coherent, λ=405 nm, max. power =50 mW) was used for photocurrent excitation. A custom-made spatial filter was designed to obtain a collimated Gaussian laser beam of 1.2 mm diameter to match with the effective area of the micro-mirror. In this design, a 4-quadrant (bi-directional on two axes) gimbal-less microelectromechanical system (MEMS) mirror

(Mirrorcle Technologies, Inc., USA) of diameter 1.6 mm was employed. A universal serial bus (USB) powered MEMS controller (USB-SL MZ, Mirrorcle Technologies, Inc., USA) provided USB communication, control of the MEMS mirror and synchronization with a lock-in amplifier. A simple two-lens beam expander combination in a 4f arrangement (scan and tube lenses) was used to expand the beam so as to overfill the back aperture of the objective lens (see Figure S1). Considering the requirements of long working distance and spherical aberration from the sample, we selected a CFI S Plan Fluor ELWD 40× objective (MO) with correction ring (Nikon, numerical aperture 0.6, Correction Collar 0-2.0 mm, working distance 2.8-3.6 mm). A mirror (M3) was used to direct the beam vertically and the sample was mounted horizontally onto an XYZ positioning system (CONEX-MFACC, Newport, UK) with 100 nm minimum incremental motion. A digital CMOS camera (ORCA-Flash4.0 LT, Hamamatsu Photonics Ltd, UK) and a white light source were integrated into the setup to allow in-situ viewing of the sample surface. Photocurrent measurements were carried out using an MFLI lock-in amplifier (Zurich Instruments). It covers the frequency range from 0 Hz (direct current, DC) to 500 kHz with fast digital processing and allows operation in both, AC (LAPS) or DC (LAE) modes. The system was controlled, and data and real-time video frames of electrochemical images were recorded using a custom-designed program written with LABVIEW (National Instruments). The setup was constructed on an optical bench (RS2000, Newport) and enclosed to avoid interference from ambient light. All measurements were carried out in a custom-built Faraday cage to minimize noise from external sources.

The setup in LAPS mode measures the localized non-faradaic AC photocurrent across the electrolyte/insulator/semiconductor structure, irradiated with a frequency-modulated laser spot at a specific position. In LAE mode, it provides information of localized faradaic electrochemistry of any region on an electrolyte/semiconductor surface addressed with a non-modulated laser spot. The setup

can uniformly scan an area of 160 µm ×160 µm (Figure S2).
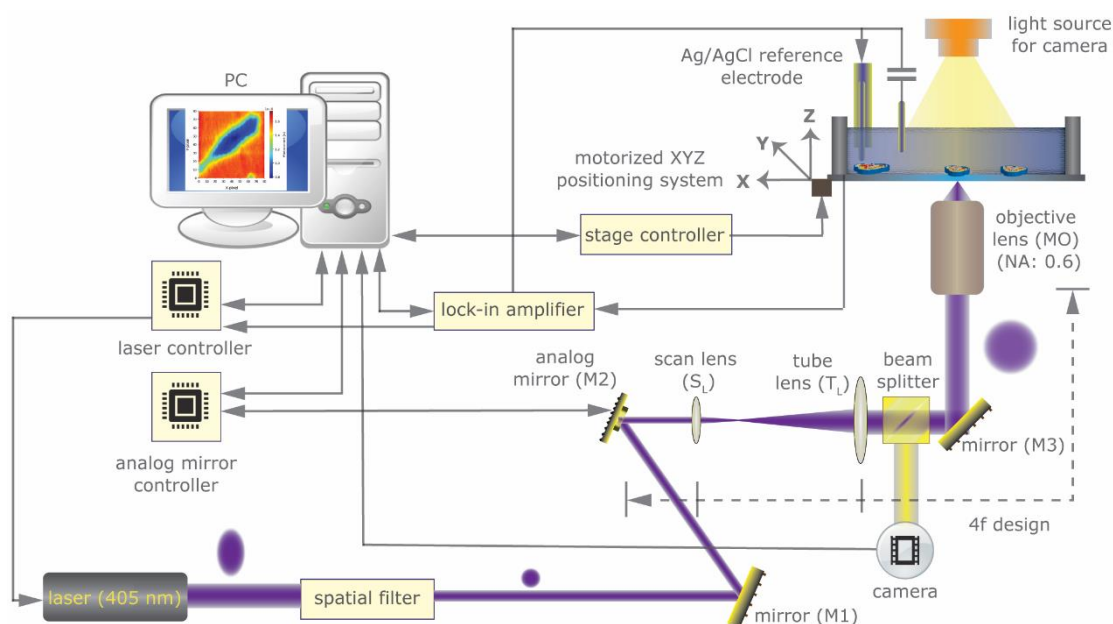
Figure 1. Schematic of the high-speed, high lateral resolution photoelectrochemical imaging setup. An analog micro-mirror based fast beam steering is achieved with 4f design lens relay system.

2.2. Materials and chemicals

Fluorine-doped tin oxide (FTO) coated glass (15 Ω/sq.) was purchased from Solaronix SA, Switzerland. Silicon on sapphire (SOS) with a 1 µm thick silicon (100) layer (boron doped, 0.1 Ω·cm) on a 475 µm thick sapphire substrate was purchased from Monocrystal, Russia. B50 rat neuroblastoma cells (Cat No 85042302) were purchased from Sigma-Aldrich. Cell culture reagents including Dulbecco's Modified Eagle's Medium (DMEM, cat no. D6046), Fetal Bovine Serum (FBS, cat no. F9665), penicillin-streptomycin (cat no. P4333), Dulbecco's Phosphate Buffered Saline (DPBS, (pH 7.4, 10 mM phosphate buffer solution containing 137 mM NaCl and 2.7 mM KCl)), and Trypsin-EDTA (cat no. T3924) were purchased from Sigma-Aldrich. LIVE/DEAD™ viability kit including Calcein AM and Ethidium homodimer-1 (Cat No. L3224) and Hoechst 33342 (Cat No. H1399) were purchased from Thermo Fisher Scientific, UK. All other chemicals were purchased from Sigma-Aldrich. All solutions were prepared using ultrapure water (18.2 MΩ·cm) from a Milli-Q

water purification system (Millipore, USA).

2.3. Sample preparation

Hematite thin films were synthesized on FTO coated glass substrates adapting an electrodeposition method described previously (Spray and Choi 2009; Zandi et al. 2016) (see supporting information (SI) for details). The as deposited FeOOH films were annealed at 550 °C for 2 h to convert FeOOH to α-Fe_2O_3 (hematite) followed by a further high-temperature anneal at 750 °C for 20 min to introduce Sn doping (Ling and Li 2014) and improve the crystallinity (Wang et al. 2017). Unless otherwise noted, the hematite films were annealed in a nitrogen (N_2) atmosphere to create oxygen vacancies (Ling et al. 2012). Under the optimized preparation conditions, an enhanced photoelectrochemical performance of hematite can be achieved by a synergistic effect of Sn doping and oxygen vacancies.

Amine-terminated SOS substrates prepared following our previously reported protocol were used for LAPS measurements (Wu et al. 2017b). Briefly, alkyne-terminated surfaces were obtained by assembling 1,8-nonadiyne monolayer on SOS through hydrosilylation, which were further functionalized with 3-azido-1-propanamine (azido-NH_2) via copper(I)-catalyzed azide alkyne cycloaddition (CuAAC) "click" chemistry.

2.4. Material characterization

The surface and cross-sectional morphology of hematite was characterized using a scanning electron microscope (SEM, FEI Inspect F). Ultraviolet–visible (UV-Vis) spectra were recorded with a UV−Vis spectrometer (PerkinElmer, Lamda 950). X-ray photoelectron spectroscopy (XPS) and ultraviolet photoelectron spectroscopy (UPS) were carried out with a Nexsa XPS system (Thermo

Scientific, UK, see SI for details).

2.5. Photocurrent measurements

Photoelectrochemical measurements in this work (LAPS, LAE and linear sweep voltammetry (LSV)) were conducted in a custom-made electrochemical cell using a platinum electrode and an Ag/AgCl electrode as the counter and reference electrodes, respectively. LSV and chronoamperometry of hematite film were carried out in pH 7.4 DPBS solution with an Autolab PGSTAT30/FRA2 (Windsor Scientific Ltd, UK) with a voltage scan rate of 5 mV/s and a diode laser ($\lambda = 405$ nm, max 50 mW) as the light source. The laser light was chopped in 10 s intervals for LSV and 0.1 s intervals for chronoamperometry with a sampling period of 0.5 ms.

## 2.6. Cell culture and cell viability test

Hematite samples and photoelectrochemical imaging chambers were sterilized with 70% ethanol, rinsed with sterilized DPBS solution and blown dry. B50 rat neuroblastoma cells were expanded in T75 cell culture flasks with DMEM supplemented with 10% FBS and 1% penicillin-streptomycin solution (S-DMEM), under standard culture conditions (SCC, humidified atmosphere with 5% CO_2 at 37°C). At confluence, cells were trypsinized, re-suspended in S-DMEM, seeded onto the hematite surface at a density of 3.2 x 10^4 cells/cm^2 and incubated under SCC for 24 hours. For photoelectrochemical imaging, S-DMEM was replaced with S-HEPES (20 mM HEPES buffer at pH 7.4, supplemented with 137 mM NaCl, 2.7 mM KCl, 1.0 mM $MgCl_2$, 0.9 mM $CaCl_2$). Cell viability was assessed via a fluorescence live/dead cell assay (see SI for details).

3. Results and discussion

3.1. Electrochemical imaging in LAPS mode with high spatiotemporal resolution

The layout of the proposed light-addressing setup, that fulfills the longstanding demand of real-time electrochemical imaging ability at faster speed with high lateral resolution, is shown in Figure 1. An analog micro-mirror served as a high-speed light addressing platform for scanning a laser beam across the back surface of the sample and was designed with a precise optical setup to obtain a diffraction limited laser spot within the scanning area.

To assess the spatial and temporal resolution of the setup, a LAPS structure based on monolayer modified SOS was investigated. To determine the lateral resolution, the sensor surface was patterned with SU-8 photoresist. A line scan from the masked to the unmasked area of the sensor surface was then carried out with a step size of 100 nm (inset of Figure 2a). The full width at half maximum (FWHM) of the 1st derivative of the fitted line which defined the lateral resolution (George et al. 2000) was calculated as 1.7 µm, which is similar to the best resolution previously reported for this wavelength (Chen et al. 2010; Wang et al. 2015).
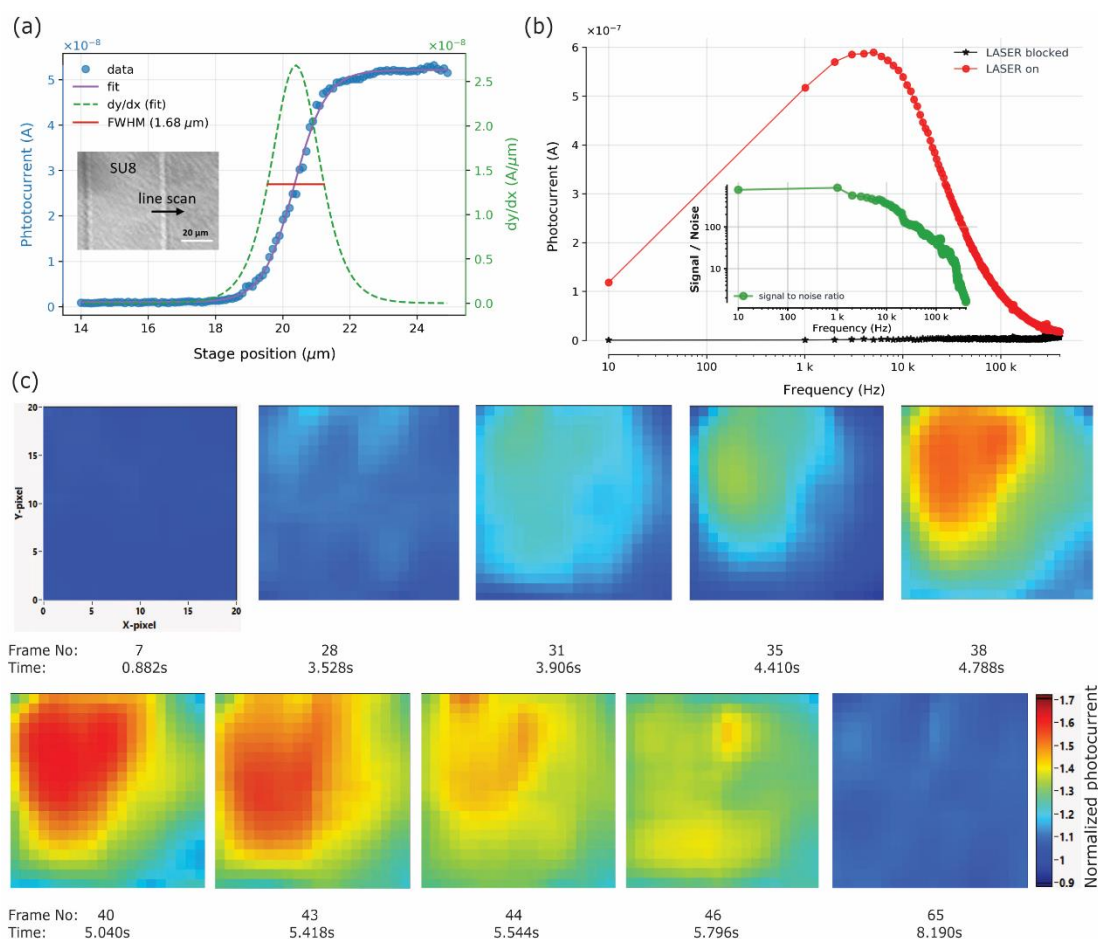
Figure 2. Performance of the photoelectrochemical imaging setup with organic monolayer modified SOS as the sensor substrate (a) Line scan across the edge of an SU-8 pattern. A lateral resolution of 1.68 μm was determined from the FWHM of the first derivative of the line scan. (b) Frequency dependence of the AC photocurrent and the background dark current measured at 0.8 V; the corresponding signal to noise ratio is shown in inset. (c) Spatiotemporal change in pH distribution was monitored at 8 frames per second after injecting 0.1 M HCl solution into a pH 7 buffer solution.

The temporal resolution of LAPS is strongly dependent on the frequency response of the sensor chip and a higher signal to noise ratio (S/N) is necessary for high-speed chemical imaging (Miyamoto et al. 2014). A frequency scan from 10 Hz to 400 kHz shows that a significant S/N (≥ 45) was obtained up to modulation frequencies of 120 kHz (Figure 2b).

A spatiotemporal change in the pH distribution caused by injecting 0.1 M HCl acid into a pH 7 buffer solution on the sensing surface (pH sensitivity 23mV/pH) was investigated to demonstrate the high-speed chemical imaging performance of the setup. A rectangular area of approximately $160{\times}160$ μm^2 in the center of the chip was scanned with a modulation frequency of 100 kHz through 20 lines

11

at a speed of 6.3 ms per line, which resulted in a frame rate of 8 frames per second (fps). A sequence of frames selected from the chemical image video (Supplementary movie M1) clearly shows temporary spreading and then shrinking of the acidic area because of the buffer action (Figure 2c).

While this demonstrates the ability of the system to visualize dynamic ion fluxes with ion-sensitive LAPS with high spatiotemporal resolution, another aim of this work was to study dynamic changes in cell attachment and permeability of the cell membrane, which can only be done with LAE. As silicon substrates require surface passivation with an organic monolayer for LAE, we developed hematite coated electrodes to construct electrochemical image of living cells by mapping the faradaic current as hematite is biocompatible and can be used without further modification.

3.2. Hematite substrate characterization

Electrodeposited FeOOH films were annealed to be converted to crystalline α-Fe_2O_3 (hematite) films as this material has a convenient bandgap for visible light absorption, high stability and biocompatibility (also see introduction). The SEM image of the as-deposited FeOOH film (Figure 3b) depicts continuous and homogeneous grains with a rough surface compared to the FTO substrate (Figure 3a). The as-deposited film is amorphous FeOOH based on a previous report (Spray and Choi 2009) and X-ray diffraction (XRD) analysis (Figure S3). After annealing (Figure 3c), the film appears compact and uniform with smooth grain surfaces, representing a crystalline Fe_2O_3 film. Aggregated crystallites and a reduced amount of grain boundaries were observed as a result of high temperature annealing. This is expected to improve the photocurrent response, as grain boundaries can act as surface recombination centers (Warren et al. 2013). The thickness of the annealed film is about 200 nm (Figure 3d). Atomic force microscopy images (AFM, Dimension Icon, Bruker, UK) (Figure S4) show that the hematite film has a uniform and smooth surface with a root-mean-square (RMS)

roughness of ~22.4 nm. The amorphous nature of the as-deposited film and the formation of hematite were confirmed by XRD and Raman; the intense (110) peak observed in the XRD pattern (Figure S3a) indicates a strong preferential orientation of the [110] axis vertical to the substrate (see detailed description in SI and Figure S3).
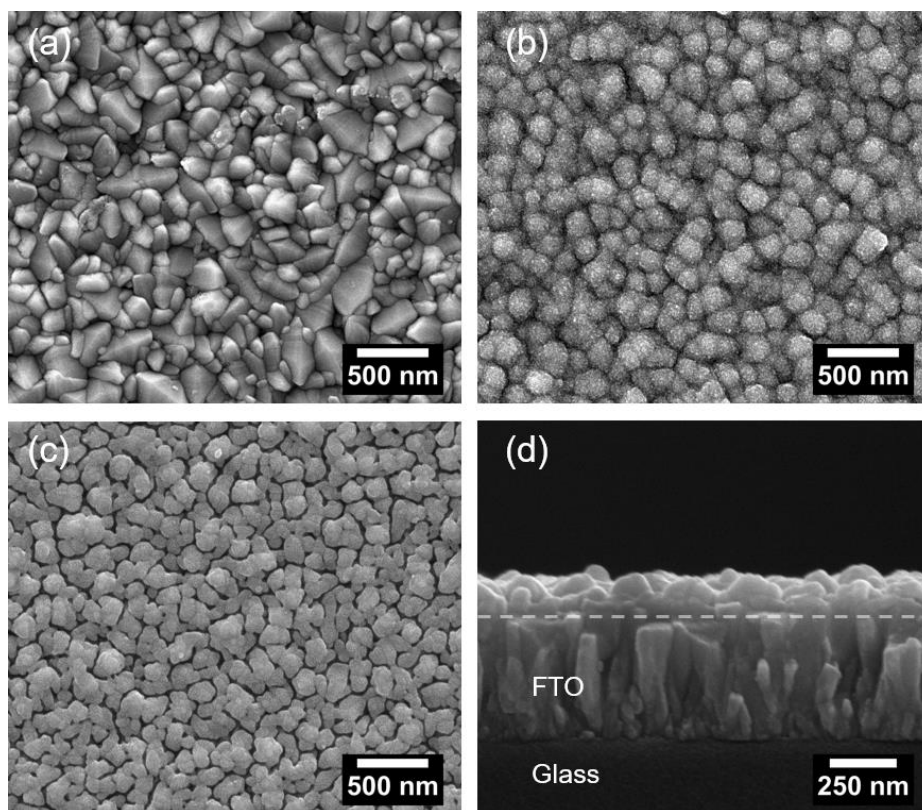
Figure 3. SEM images of (a) FTO substrate; (b) as-deposited film; (c) annealed hematite film; (d) cross-sectional view of annealed hematite film.

The surface chemistry of the prepared films was investigated by XPS measurements, which indicated that Sn^{4+} ions were incorporated into hematite during the annealing process (see SI for description and Figure S5).

A direct band gap of 2.1 eV was determined from UV−Vis spectroscopy of hematite films (Figure S6a) indicating that charge carriers can be facilely induced using a 405 nm diode laser in our PEIS. From a Mott−Schottky plot of a hematite film (Figure S6b), a donor density of 2.09×10^{18} cm^{-1} and flat band potential (E_{fb}) of -0.02 V vs. Ag/AgCl were calculated. The valence band information

was determined by UPS measurement (Figure S6c). By subtracting the width between the secondary electron cut-off energy and the valence band onset energy from the incident photon energy, the valence band maximum (VBM) energy level of -7.0 eV was obtained. Based on VBM energy level and the optical bandgap from UV-Vis spectrum, the energy diagram of the hematite electrode was calculated (Figure S6d). Considering that E_{fb} = -0.02 V, under photoelectrochemical imaging conditions (0.8 V vs. Ag/AgCl), the main reaction is the oxidation of hydroxide ions to hydroxyl radicals (*OH·*) (Jaeger and Bard 1979). Characterization of the hematite films with electrochemical impedance spectroscopy (EIS) demonstrates the decrease of the charge transfer resistance with illumination (see description in SI and Figure S7).
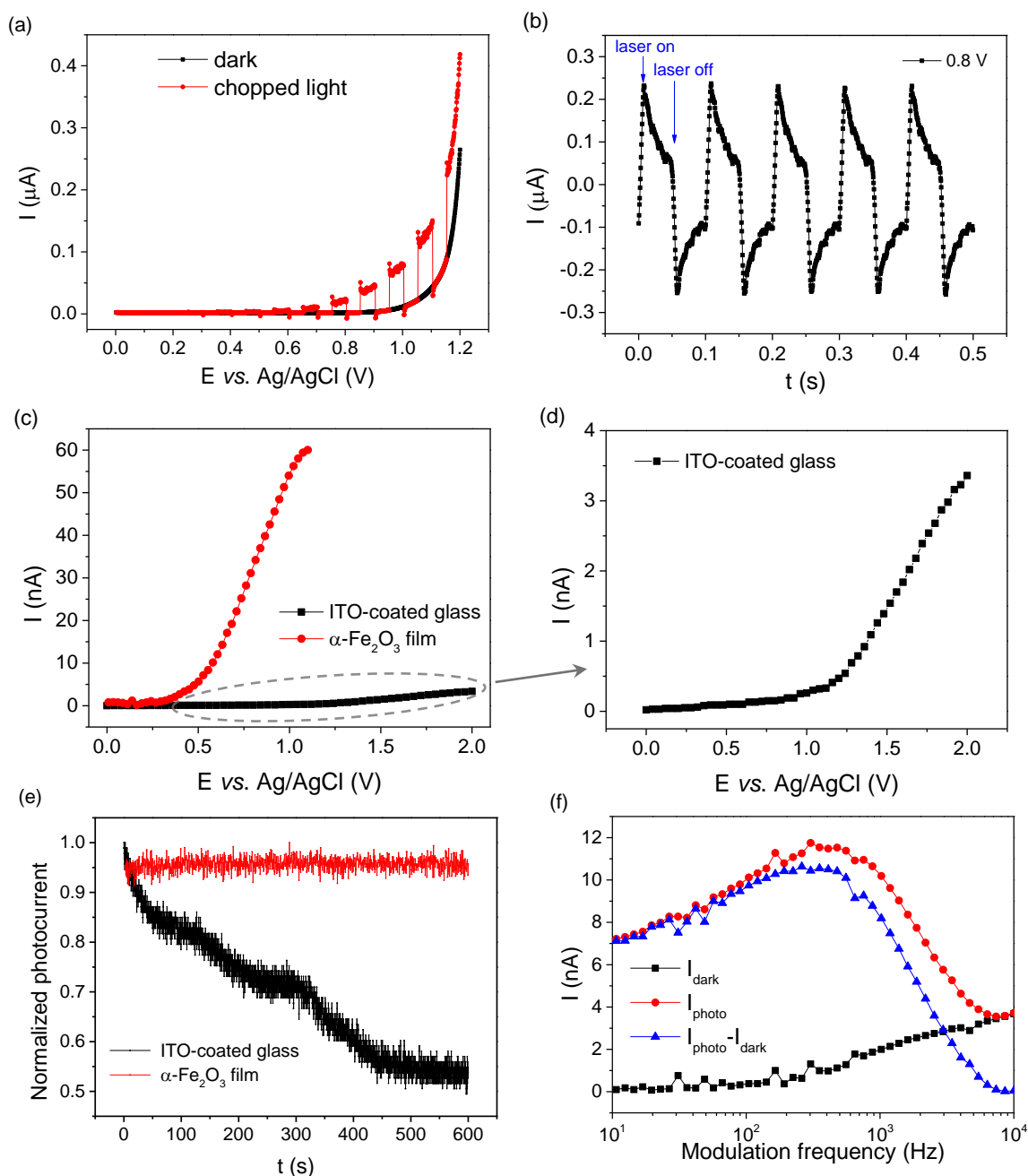
3.3. Photocurrent response of hematite films

LSVs of hematite films with chopped illumination showed a negligible dark current over a large potential range, which started to increase from 0.82 V, while the photocurrent had an onset potential of about 0.1 V (Figure 4a), slightly greater than the E_{fb}, indicating that an increased concentration of minority carriers facilitates oxidation reactions when a depleted electrode is under supra-bandgap illumination. 0.8 V was chosen for photocurrent imaging as a relatively low voltage that yields high photocurrent with negligible dark current. Chronoamperometry of a hematite film measured at 0.8 V with chopped laser illumination (Figure 4b) showed a rapid increase of current upon illumination (8 ms to reach the maximum photocurrent) indicating that good temporal resolution can be achieved with hematite films. Moreover, the photocurrent is a combination of faradaic and capacitive currents. The transient spikes in photocurrent upon illumination represent the accumulation of holes at the electrode/electrolyte interface without injection to the electrolyte (Dotan et al. 2011); then the photocurrent levels off to the value of redox current until light off, and subsequently negative spikes

occurred, representing the recombination of charge carriers.

The performance of the hematite developed in this work was compared with that of ITO previously employed for photoelectrochemical imaging (Wu et al. 2019; Zhang et al. 2017). AC photocurrent-voltage (*I-V*) curves of hematite films (Figure 4c) showed an increasing photocurrent with the applied voltage and reached a plateau of about 60 nA at 1.1 V, which was around 18 times larger than the maximum photocurrent of ITO (Figure 4d). With the working voltage reduced to half and the photocurrent signal increasing dramatically, the hematite film overwhelmingly outplays ITO in photocurrent response. Photocurrent stability measured at constant voltages with hematite films and ITO (voltages were chosen in similar working regions in *I-V* curves, 0.8 V and 1.5 V for hematite film and ITO respectively) showed a continuous decrease to 53% of its maximum value in 10 min for ITO, while the hematite film did not suffer from any photocurrent degradation over 10 min, showing an excellent stability for measuring subtle changes when used in imaging (Figure 4e).

The frequency dependence of the photocurrent measured with hematite films (Figure 4f) showed a net photocurrent increase with frequency and reached a maximum at 200 ~ 500 Hz, then decreased and became negligible from 5 kHz. In contrast, the AC photocurrent measured with ITO previously decreased continuously with increasing modulation frequency above 10 Hz, i.e. photoelectrochemical imaging can be performed at higher frequencies with hematite than with ITO. The maximum modulation frequency that offers a good S/N with hematite is about 1 kHz. While this is a considerable improvement compared to ITO, it will significantly reduce the imaging speeds compared to the LAPS measurements with SOS substrates demonstrated above (Figure 2).

Figure 4. Photocurrent response of hematite films (a) LSV and (b) chronoamperometry of hematite film measured at 0.8 V in pH 7.4 DPBS. (c) Comparison of AC *I-V* curves of hematite film and ITO-coated glass in pH 7.4 DPBS with a focused laser beam and a light modulation of 10 Hz; (d) Rescaled plot of the *I-V* curve of ITO-coated glass; (e) AC photocurrent-time (*I-t*) curves of hematite film and ITO-coated glass over 600 s in pH 7.4 DPBS with a focused laser beam and a light modulation of 10 Hz; (f) Frequency dependence of the AC photocurrent and the background dark current of hematite film measured at 0.8 V with a focused laser beam in pH 7.4 DPBS.

3.4. Dynamic monitoring of cellular responses to Triton X-100 (TX-100) in LAE mode:

To facilitate dynamic imaging with the hematite substrates in our new setup, the imaging speed had to be optimized. Previously, cell imaging with PEIS was carried out with AC modulated light intensity in a mechanical scanning system requiring 7 min to record a 2.5k pixel image using ITO or InGaN substrates (Wu et al. 2019; Zhou et al. 2019). The maximum frame rate that can be achieved in the new setup with this AC technique for a 2.5k pixel image is 50 s per frame (Figure S8a) as the modulation frequency of a maximum value of 1 kHz with the hematite electrode (see above) restricted the data transfer rate up to 52 data points per second. A significant increase of the data transfer rate up to 418 data points per second (Figure S8b) was achieved by measuring DC photocurrent instead of AC photocurrent which enabled construction of a 14.4k pixel image within 36 s (Figure S8c).

In order to test the performance of the system, cellular responses to permeabilization with TX-100 were monitored with the hematite electrodes. TX-100 is a widely used surfactant for lysing cells to extract protein or organelles, or for permeabilizing the membranes of living cells (Koley and Bard 2010; le Maire et al. 2000; Paternostre et al. 1988; van de Ven et al. 2009). When the concentration of TX-100 is far below the critical micelle concentration (CMC, 0.19 to 0.24 mM (Koley and Bard 2010; Morandat and El Kirat 2006)), the effect on membrane permeability would be negligible; when it is slightly lower than CMC, cell membranes become permeable allowing hydrophilic molecules to pass through, but cells are able to recover from this disruption after the surfactant has been removed (van de Ven et al. 2009). When the concentration is higher than CMC, irreversible permeabilization of cell membranes occurs due to substantial insertion of surfactant molecules into membranes, disrupting the lipid bilayer, solubilizing membrane-bound proteins, and ultimately demolishing the cellular structure (Danielsen and Hansen 2017; Vaidyanathan et al. 2014). For comparison with photocurrent imaging, fluorescence images of B50 cells were recorded when cells were exposed to

TX-100 in parallel experiments.

Photocurrent images (each frame containing 14.4k pixels and taking 36 s to record) of multiple B50 cells were taken continuously to generate videos. Figure 5a shows a sequence of images from a photocurrent video (Supplementary movie M2) of B50 cells before, during and after exposure to 0.01% (*v/v*) TX-100 (0.17 mM) in supplemented HEPES buffer (S-HEPES). Before exposure to TX-100 (frame 9), intact cell membrane profiles and some cell processes are clearly visible. The photocurrent under the cells was lower than on the blank surface, and the photocurrent in cell centers was lower than along the cell edges as the narrow gap between the cells and the hematite surface limited the diffusion of hydroxide to the surface (Wu et al. 2019). S-HEPES buffer was replaced with 0.01% TX-100 in S-HEPES buffer at frame 10 (6 min). From frame 10 to 30 (18 min), the photocurrent under the cells gradually increased while cell profiles remained the same. In a similar time frame (10 min), leakage of cytoplasm through cell membrane and membrane blebbing were observed in the fluorescence image (Figure S9a) in accordance with a previous report where cytoplasm leakage resulted from permeabilization of the membrane in response to TX-100, and the formation of blebs was attributed to local rupture of the actin cortex or local detachment of the membrane from the cytoskeleton (Charras and Paluch 2008). The increased permeability of the cell membrane will also allow diffusion of ions, resulting in the observed increase of the photocurrent under the cells. At frame 60 (36 min), photocurrent values under the cells continued to increase, and other changes appeared in the photocurrent image including the shrinkage of cell profiles (cells A, C, D and E) and the disappearance of cell B and some cell processes. The disappearance of cell B is most likely linked to cell death as cell B appears rounded with indistinct edges in the optical image after the experiment, and the disappearance of photocurrent contrast under cells has previously been linked to cell death (Wu et al. 2019). The likelihood of cell death was also confirmed by cytotoxicity experiments in

Figure S10a. For 0.01% TX-100 in S-HEPES, viability decreased slowly with time to 94.19% ± 1.61% at 40 min and 83.07% ± 6.82% at 60 min, i.e. TX-100 at a concentration below CMC causes mild disruption to cell membranes, but prolonged exposure was detrimental to cell viability. The shrinkage of cell profiles in the photocurrent image was not linked to shrinkage of cells in the optical (Figure 5a) and fluorescence images (Figure S9a) and therefore most likely reflects diffusion driven penetration of HEPES into cell bodies on permeabilization of the membrane after prolonged exposure to 0.01% TX-100 in S-HEPES buffer. The disappearance of cell processes could not be linked to equivalent changes in the fluorescent images. It is therefore assumed that the cell processes are more likely to become detached from the substrate allowing ions to diffuse more freely to the hematite surface. The 0.01% TX-100 in S-HEPES buffer was replaced by fresh HEPES buffer at frame 102 (61 min). After that, photocurrents under the cells (cells A, C, D and E) started to recover and at frame 170 (102 min), photocurrents under cells C, D and E recovered approximately to their original values, while cell A showed incomplete recovery. In contrast to photocurrent imaging, the cells looked fully recovered even before removal of TX-100 in the 50 min fluorescence image (Figure S9a), which could be due to the reformation of an actomyosin cortex, followed by bleb retraction (Blaser et al. 2006). After removal of TX-100, the cell morphologies in the fluorescence images remained unchanged (80 min image in Figure S9a). The fluorescence images of most of the cells at 0 min (in S-HEPES), 50 min (45 min after introduction of 0.01% TX-100) and 80 min (30 min after removal of TX-100) show similar morphology, even though the photocurrent values and profiles under cells in the parallel photocurrent experiment showed significant differences at these times. This indicates that photocurrent imaging provides information about changes in the cell viability linked to changes in membrane permeability and quality of cell attachment under the influence of TX-100 that are not visible in fluorescence images. Moreover, the heterogeneity of the cell responses to 0.01% TX-100

in S-HEPES buffer is shown more clearly in the time-dependent profiles of photocurrents from cell-attachment regions (Figure 5b). Although photocurrents under the cells all increased after 0.01% TX-100 was added and reached plateaus at around frames 80-100 and then were able to recover after replacing 0.01% TX-100 with fresh buffer, the rate and magnitude of photocurrent change varied from cell to cell. Photocurrents under cells C, D and E had relatively low plateaus, and they were able to recover to initial values, which shows that these cells were more resilient and less affected by 0.01% TX-100, while cell A was more disrupted by permeabilization of the lipid membrane and cell B suffered a complete breakdown of its cell membrane. Normalized photocurrent line scans through cells C and D (Y = 79 in photocurrent images in Figure 5a) in Figure 5c clearly show that the minimum photocurrents under these two cells recovered completely, while the apparent cell-attachment areas (widths) only recovered to some extent, which indicates a partial recovery from temporary damage of the cell membranes after replacing buffer containing 0.01% TX-100 with fresh S-HEPES. This is also confirmed by the optical image after the scan that shows a disruption or detachment of the processes while the shape and size of the cell remains the same. These results are in agreement with previously published data that showed concentration dependent reversible permeabilization of mammalian cell membranes using TX-100 and recovery of cell metabolism after removal of TX-100 (van de Ven et al. 2009).

Figure 6a depicts the sequence of photocurrent cell images captured from a photocurrent video (Supplementary movie M3) when cells were exposed to 0.02% (*v/v*) TX-100 in S-HEPES buffer, a concentration above CMC. It is obvious that the photocurrents under all the cells increased with time after replacing S-HEPES with 0.02% TX-100 in S-HEPES, and cell profiles vanished at frames 22-60 (13-36 min). This is in agreement with the results of fluorescence imaging (Figure S9b). Cells swelled and became round within 10 min after exposure to 0.02% TX-100 in S-HEPES, which

indicates the toxicity of TX-100 with a concentration above CMC as cell membranes were solubilized and rapidly lost their compactness and integrity. The results are in agreement with previously published data that showed irreversible permeabilization of cell membranes due to exposure of TX-100 concentrations greater than the CMC (Vaidyanathan et al. 2014). Cytotoxicity experiments also confirmed that cell viability dropped sharply at a TX-100 concentration of 0.02%; only about 1% cells were viable after 60 min exposure (Figure S10a). Similarly, time-dependent profiles (Figure 6b) and line scans (Figure 6c) showed that photocurrents under cells increased to higher values closer to the background photocurrent reaching their maximum values in shorter times (40-60 frames) than for cells treated with 0.01% TX-100 in S-HEPES (see comparison of time dependent photocurrent in Figure S11), which is in agreement with the loss of cellular integrity and viability shown in the optical images (Figure S9b).

Negative control experiments were carried out to rule out other factors that might cause damage to the cells (Supplementary movie M4). Cell profiles and photocurrent values under cells recorded in S-HEPES buffer were stable over more than 120 frames (72 min) (Figure S12a and c), though the photocurrent values varied from cell to cell reflecting sensitivity to individual cellular status within the population (Figure S12b). Negative control experiments carried out using fluorescence microscopy also confirmed the stability of the cells in S-HEPES buffer (Figure S9c) as almost no change occurred in cell images over 60 min. Similarly, investigation of cell viability on exposure to TX-100 and under negative control conditions (Figure S10a) revealed that more than 99% of cells were viable when incubated in S-HEPES buffer on the hematite substrate for over 60 min if no surfactant was applied, confirming the good biocompatibility and biosafety of hematite photoanodes for use in *in vitro* applications reported previously (Kim et al. 2017).
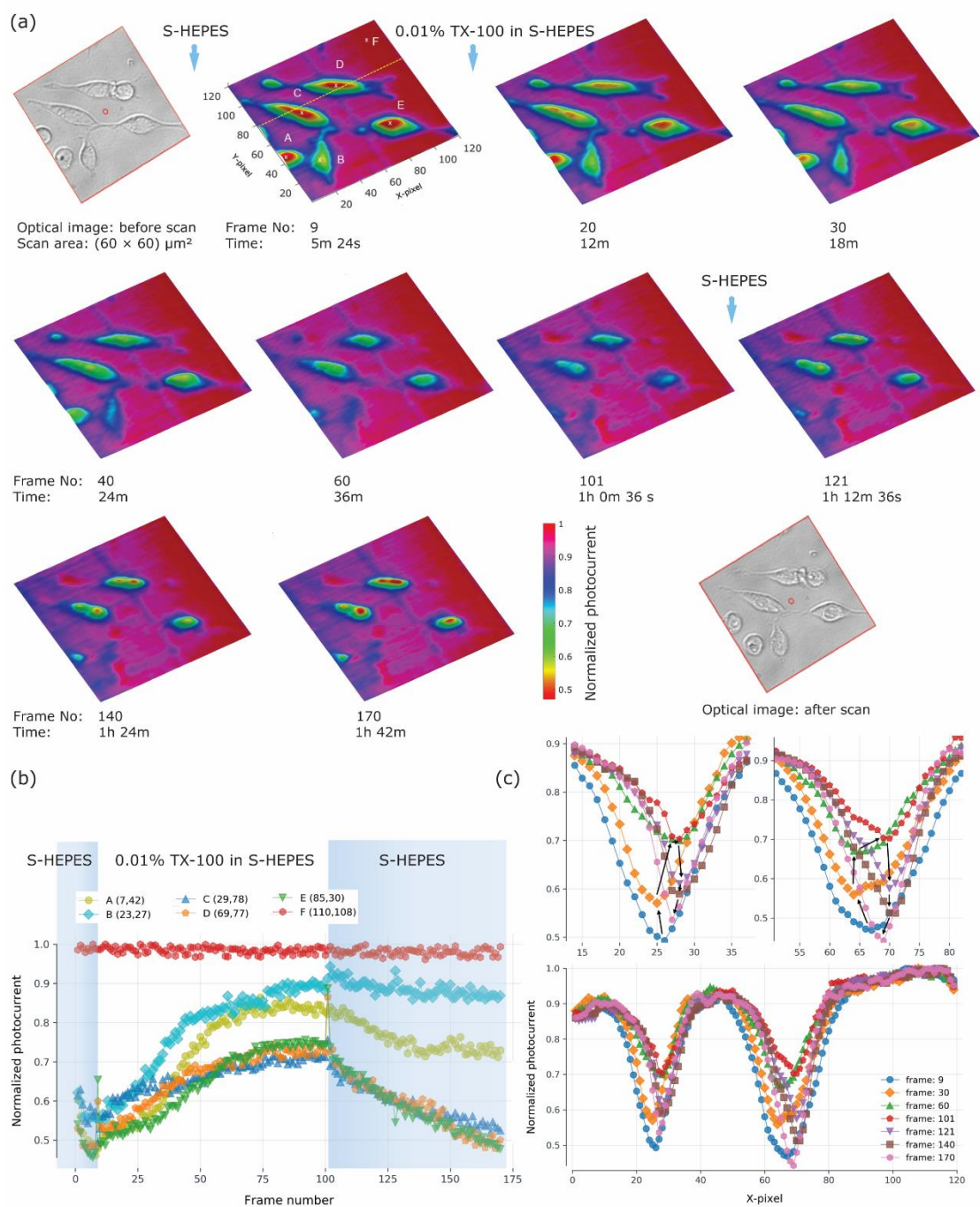
Figure 5. Photocurrent changes under cells during exposure to a TX-100 concentration smaller than the critical micelle concentration (a) time-lapse photocurrent images of B50 cells exposed to 0.01% TX-100 in S-HEPES buffer, (b) time-dependent photocurrent traces for individual cells, (c) photocurrent X-axis line scan analysis.
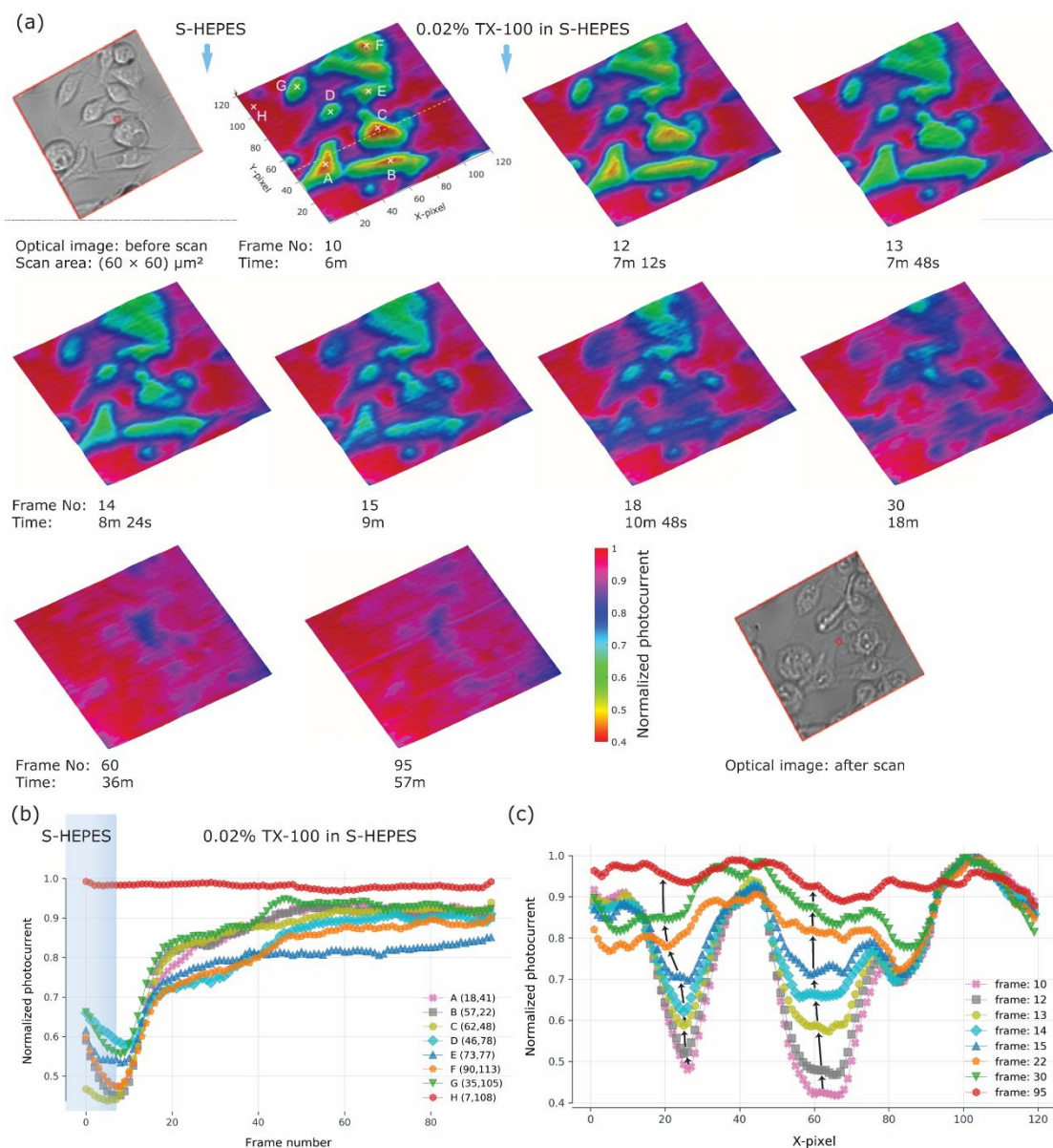
Figure 6. Photocurrent changes under cells during exposure to a TX-100 concentration greater than the critical micelle concentration (a) time-lapse photocurrent images of B50 cells exposed to 0.02% TX-100 in S-HEPES buffer, (b) time-dependent photocurrent traces for individual cells, (c) photocurrent X-axis line scan analysis.

4. Conclusions

A new photoelectrochemical imaging system (PEIS) with high spatiotemporal resolution was presented. By using an analog micro-mirror to scan the sensor surface in conjunction with a precise optical setup to obtain a diffraction limited laser spot, this versatile system is capable of conducting ultra-high speed LAPS measurement based on electrolyte-insulator-semiconductor structures as well

as high-speed AC/DC photoelectrochemical imaging based on electrolyte- semiconductor structures with excellent lateral resolution. With imaging speeds of up to 8 fps, the PEIS lends itself for the investigation of the kinetics of localized electrochemical reactions and changes in ion concentrations and continuous monitoring of biological processes in *in-vitro* cell cultures with subcellular resolution.

Hematite thin films were shown to be excellent sensor substrates for continuous photocurrent imaging of living cells, exhibiting high photocurrents, good stability, excellent spatial resolution and good biocompatibility. The ability of the new PEIS setup together with hematite substrates to monitor cellular processes was demonstrated by continuously mapping the responses of B50 cells to the surfactant TX-100. Photocurrent changes observed during the exposure of the cells to TX-100 could be directly linked to changes in the permeability of the cell membrane to hydrophilic species such as ions and to changes in the cell-surface attachment area. The PEIS showed the dynamics of the permeabilization and recovery of the cell membrane and thus cell viability in much greater detail than could be visualized with fluorescent microscopy. In addition to gaining detailed insights into the dynamics of the cell-surface interface, the PEIS will also lend itself for the monitoring of ion and metabolite concentrations providing information that cannot be easily accessed by other techniques thereby forming a useful auxiliary to light-microscopy. The advantage of this PEIS over other electrochemical imaging setups is its capability to image multiple cells simultaneously and continuously, which shows the heterogeneity of cell responses and will lend itself for the investigation of statistically significant cell responses to various stimuli in the future. It is envisaged that further improvements in the imaging speeds can be achieved by developing electrodes with higher charge carrier mobility.

Acknowledgements

Supplementary material contains:

- The schematic of beam steering in the laser scanning setup
- The deflection of the laser spot depending on the amplitude applied to the micromirror device
- Electrodeposition of hematite films
- Characterization of hematite films with XRD and Raman
- Characterization of hematite films with AFM
- Characterization of hematite films with XPS and UPS
- Characterization of hematite films with EIS
- Comparison of AC and DC photocurrent images at different scanning speeds
- Fluorescence images of B50 cells exposed to different concentrations of TX-100 in S-HEPES
- Fluorescence based cell viability experiments at different concentrations of TX-100 in S-HEPES
- Normalized photocurrent changes under cells at different concentrations of TX-100 in S-

HEPES

- Negative control experiment

Movies:

- M1_phdynamics_8fps.mp4: Movie of LAPS photocurrent response upon injection of 0.1 M HCl into a pH 7 buffer solution shown in real time at 8 fps.

- M2_Recovery_5fps.mp4: Movie showing DC photocurrent images before, during and after exposure of B50 cells to 0.01% TX-100 in S-HEPES shown with 5 fps.

- M3_cell_death_5fps.mp4: Movie showing DC photocurrent images before, during and after exposure of B50 cells to 0.02% TX-100 in S-HEPES shown with 5 fps.

- M4_Control_5fps.mp4: Movie showing DC photocurrent images of B50 cells in a negative control experiment in S-HEPES shown with 5 fps.

References

Arai, T., Nishijo, T., Matsumae, Y., Zhou, Y., Ino, K., Shiku, H., Matsue, T., 2013. Noninvasive Measurement of Alkaline Phosphatase Activity in Embryoid Bodies and Coculture Spheroids with Scanning Electrochemical Microscopy. Anal. Chem. 85(20), 9647-9654.

Bard, A.J., Fan, F.R.F., Kwak, J., Lev, O., 1989. Scanning electrochemical microscopy. Introduction and principles. Anal. Chem. 61(2), 132-138.

Bergner, S., Wegener, J., Matysik, F.-M., 2011. Simultaneous Imaging and Chemical Attack of a Single Living Cell within a Confluent Cell Monolayer by Means of Scanning Electrochemical Microscopy. Anal. Chem. 83(1), 169-174.

Blaser, H., Reichman-Fried, M., Castanon, I., Dumstrei, K., Marlow, Florence L., Kawakami, K., Solnica-Krezel, L., Heisenberg, C.-P., Raz, E., 2006. Migration of Zebrafish Primordial Germ Cells: A Role for Myosin Contraction and Cytoplasmic Flow. Dev. Cell 11(5), 613-627.

Bohn, C.D., Agrawal, A.K., Walter, E.C., Vaudin, M.D., Herzing, A.A., Haney, P.M., Talin, A.A., Szalai, V.A., 2012. Effect of Tin Doping on α-Fe$_2$O$_3$ Photoanodes for Water Splitting. J. Phys. Chem. C 116(29), 15290-15296.

Charras, G., Paluch, E., 2008. Blebs lead the way: how to migrate without lamellipodia. Nat. Rev. Mol. Cell Biol. 9(9), 730-736.

Chen, C.C., Zhou, Y., Baker, L.A., 2012. Scanning ion conductance microscopy. Annu. Rev. Anal. Chem. 5, 207-228.

Chen, L., Zhou, Y., Jiang, S., Kunze, J., Schmuki, P., Krause, S., 2010. High resolution LAPS and SPIM. Electrochem. Commun. 12(6), 758-760.

Choudhury, M.H., Ciampi, S., Yang, Y., Tavallaie, R., Zhu, Y., Zarei, L., Goncales, V.R., Gooding, J.J., 2015. Connecting electrodes with light: one wire, many electrodes. Chem. Sci. 6(12), 6769-6776.

Danielsen, E.M., Hansen, G.H., 2017. Intestinal surfactant permeation enhancers and their interaction with enterocyte cell membranes in a mucosal explant system. Tissue Barriers 5(3), e1361900.

Das, A., Chen, T.-C., Yang, C.-M., Lai, C.-S., 2014a. A high-speed, flexible-scanning chemical imaging system using a light-addressable potentiometric sensor integrated with an analog micromirror. Sens. Actuators, B 198, 225-232.

Das, A., Das, A., Chang, L.B., Lai, C.S., Lin, R.M., Chu, F.C., Lin, Y.H., Chow, L., Jeng, M.J., 2013. GaN Thin Film Based Light Addressable Potentiometric Sensor for pH Sensing Application. Appl. Phys. Express 6(3), 036601.

Das, A., Lin, Y.-H., Lai, C.-S., 2014b. Miniaturized amorphous-silicon based chemical imaging sensor system using a mini-projector as a simplified light-addressable scanning source. Sens. Actuators, B 190, 664-672.

Das, A., Yang, C.-M., Chen, T.-C., Lai, C.-S., 2015. Analog micromirror-LAPS for chemical imaging and zoom-in application. Vacuum 118, 161-166.

Decelle, J., Veronesi, G., Gallet, B., Stryhanyuk, H., Benettoni, P., Schmidt, M., Tucoulou, R., Passarelli, M., Bohic, S., Clode, P., Musat, N., 2020. Subcellular Chemical Imaging: New Avenues in Cell Biology. Trends Cell Biol. 30(3), 173-188.

Dotan, H., Sivula, K., Grätzel, M., Rothschild, A., Warren, S.C., 2011. Probing the photoelectrochemical properties of hematite (α-Fe$_2$O$_3$) electrodes using hydrogen peroxide as a hole scavenger. Energy Environ. Sci. 4(3), 958-964.

George, M., Parak, W.J., Gerhardt, I., Moritz, W., Kaesen, F., Geiger, H., Eisele, I., Gaub, H.E., 2000. Investigation of the spatial resolution of the light-addressable potentiometric sensor. Sens. Actuators, A 86(3), 187-196.

Giepmans, B.N.G., Adams, S.R., Ellisman, M.H., Tsien, R.Y., 2006. The Fluorescent Toolbox for Assessing Protein Location and Function. Science 312(5771), 217.

Hafeman, D.G., Parce, J.W., McConnell, H.M., 1988. Light-addressable potentiometric sensor for biochemical systems. Science 240(4856), 1182.

Hansma, P.K., Drake, B., Marti, O., Gould, S.A., Prater, C.B., 1989. The scanning ion-conductance microscope. Science 243(4891), 641.

Jaeger, C.D., Bard, A.J.J.J.o.P.C., 1979. Spin trapping and electron spin resonance detection of radical intermediates in the photodecomposition of water at titanium dioxide particulate systems. J. Phys. Chem. 83(24), 3146-3152.

Jiang, C., Moniz, S.J.A., Wang, A., Zhang, T., Tang, J., 2017. Photoelectrochemical devices for solar water splitting - materials and challenges. Chem. Soc. Rev. 46(15), 4645-4660.

Kennedy, J.H., 1978. Flatband Potentials and Donor Densities of Polycrystalline α-Fe$_2$O$_3$ Determined from Mott-Schottky Plots. J. Electrochem. Soc. 125(5), 723.

Kim, K., Lee, B.I., Chung, Y.J., Choi, W.S., Park, C.B., 2017. Hematite-Based Photoelectrode Materials for Photoelectrocatalytic Inhibition of Alzheimer's β-Amyloid Self-Assembly. Advanced Healthcare Materials 6(8), 1601133.

Koley, D., Bard, A.J., 2010. Triton X-100 concentration effects on membrane permeability of a single HeLa cell by scanning electrochemical microscopy (SECM). Proc. Natl. Acad. Sci. U. S. A. 107(39), 16783-16787.

le Maire, M., Champeil, P., Møller, J.V., 2000. Interaction of membrane proteins and lipids with solubilizing detergents. Biochim. Biophys. Acta, Biomembr. 1508(1), 86-111.

Ling, Y., Li, Y., 2014. Review of Sn-Doped Hematite Nanostructures for Photoelectrochemical Water Splitting. Part. Part. Syst. Charact. 31(11), 1113-1121.

Ling, Y., Wang, G., Reddy, J., Wang, C., Zhang, J.Z., Li, Y., 2012. The influence of oxygen content on the thermal activation of hematite nanowires. Angew. Chem. Int. Ed. Engl. 51(17), 4074-4079.

Liu, X.-W., Yang, Y., Wang, W., Wang, S., Gao, M., Wu, J., Tao, N., 2017. Plasmonic-Based Electrochemical Impedance Imaging of Electrical Activities in Single Cells. Angew. Chem., Int. Ed. 56(30), 8855-8859.

Miyamoto, K.-i., Itabashi, A., Wagner, T., Schöning, M.J., Yoshinobu, T., 2014. High-speed chemical imaging inside a microfluidic channel. Sens. Actuators, B 194, 521-527.

Morandat, S., El Kirat, K., 2006. Membrane Resistance to Triton X-100 Explored by Real-Time Atomic Force Microscopy. Langmuir 22(13), 5786-5791.

Parker, S.G., Yang, Y., Ciampi, S., Gupta, B., Kimpton, K., Mansfeld, F.M., Kavallaris, M., Gaus, K., Gooding, J.J., 2018. A photoelectrochemical platform for the capture and release of rare single cells. Nat. Commun. 9(1), 2288.

Paternostre, M.T., Roux, M., Rigaud, J.L., 1988. Mechanisms of membrane protein insertion into liposomes during reconstitution procedures involving the use of detergents. 1. Solubilization of large unilamellar liposomes (prepared by reverse-phase evaporation) by Triton X-100, octyl glucoside, and sodium cholate. Biochemistry 27(8), 2668-2677.

Perry, D., Paulose Nadappuram, B., Momotenko, D., Voyias, P.D., Page, A., Tripathi, G., Frenguelli, B.G., Unwin, P.R., 2016. Surface Charge Visualization at Viable Living Cells. J. Am. Chem. Soc. 138(9), 3152-3160.

Phuan, Y.W., Ong, W.-J., Chong, M.N., Ocon, J.D., 2017. Prospects of electrochemically synthesized hematite photoanodes for photoelectrochemical water splitting: A review. J. Photochem. Photobiol. C Photochem. Rev. 33, 54-82.

Polcari, D., Dauphin-Ducharme, P., Mauzeroll, J., 2016. Scanning Electrochemical Microscopy: A Comprehensive Review of Experimental Parameters from 1989 to 2015. Chem. Rev. 116(22), 13234-13278.

Ryu, G.M., Lee, M., Choi, D.S., Park, C.B., 2015. A hematite-based photoelectrochemical platform for visible light-induced biosensing. J. Mater. Chem. B 3(22), 4483-4486.

Seo, D., Lim, S.Y., Lee, J., Yun, J., Chung, T.D., 2018. Robust and High Spatial Resolution Light Addressable Electrochemistry Using Hematite (α-Fe$_2$O$_3$) Photoanodes. ACS Appl. Mater. Interfaces 10(39), 33662-33668.

Spray, R.L., Choi, K.-S., 2009. Photoactivity of Transparent Nanocrystalline Fe$_2$O$_3$ Electrodes Prepared via Anodic

Electrodeposition. Chem. Mater. 21(15), 3701-3709.

Stephens, D.J., Allan, V.J., 2003. Light Microscopy Techniques for Live Cell Imaging. Science 300(5616), 82.

Sun, P., Laforge, F.O., Mirkin, M.V., 2007. Scanning electrochemical microscopy in the 21st century. Phys. Chem. Chem. Phys. 9(7), 802-823.

Tamirat, A.G., Rick, J., Dubale, A.A., Su, W.N., Hwang, B.J., 2016. Using hematite for photoelectrochemical water splitting: a review of current progress and challenges. Nanoscale Horiz. 1(4), 243-267.

Vaidyanathan, S., Orr, B.G., Banaszak Holl, M.M., 2014. Detergent Induction of HEK 293A Cell Membrane Permeability Measured under Quiescent and Superfusion Conditions Using Whole Cell Patch Clamp. The Journal of Physical Chemistry B 118(8), 2112-2123.

van de Ven, A.L., Adler-Storthz, K., Richards-Kortum, R., 2009. Delivery of optical contrast agents using Triton-X100, part 1: reversible permeabilization of live cells for intracellular labeling. J. Biomed. Opt. 14(2), 021012-021012.

Vogel, Y.B., Gooding, J.J., Ciampi, S., 2019. Light-addressable electrochemistry at semiconductor electrodes: redox imaging, mask-free lithography and spatially resolved chemical and biological sensing. Chem. Soc. Rev. 48(14), 3723-3739.

Wang, D., Chen, Y., Zhang, Y., Zhang, X., Suzuki, N., Terashima, C., 2017. Boosting photoelectrochemical performance of hematite photoanode with TiO_2 underlayer by extremely rapid high temperature annealing. Appl. Surf. Sci. 422, 913-920.

Wang, J., Zhou, Y., Watkinson, M., Gautrot, J., Krause, S., 2015. High-sensitivity light-addressable potentiometric sensors using silicon on sapphire functionalized with self-assembled organic monolayers. Sens. Actuators, B 209, 230-236.

Wang, W., Foley, K., Shan, X., Wang, S., Eaton, S., Nagaraj, V.J., Wiktor, P., Patel, U., Tao, N., 2011. Single cells and intracellular processes studied by a plasmonic-based electrochemical impedance microscopy. Nat. Chem. 3(3), 249-255.

Warren, S.C., Voitchovsky, K., Dotan, H., Leroy, C.M., Cornuz, M., Stellacci, F., Hebert, C., Rothschild, A., Gratzel, M., 2013. Identifying champion nanostructures for solar water-splitting. Nat. Mater. 12(9), 842-849.

Wu, F., Campos, I., Zhang, D.-W., Krause, S., 2017a. Biological imaging using light-addressable potentiometric sensors and scanning photo-induced impedance microscopy. Proc. R. Soc. A 473(2201), 20170130.

Wu, F., Zhang, D.W., Wang, J., Watkinson, M., Krause, S., 2017b. Copper Contamination of Self-Assembled Organic Monolayer Modified Silicon Surfaces Following a "Click" Reaction Characterized with LAPS and SPIM. Langmuir 33(13), 3170-3177.

Wu, F., Zhou, B., Wang, J., Zhong, M., Das, A., Watkinson, M., Hing, K., Zhang, D.W., Krause, S., 2019. Photoelectrochemical Imaging System for the Mapping of Cell Surface Charges. Anal. Chem. 91(9), 5896-5903.

Yoshinobu, T., Iwasaki, H., Nakao, M., Nomura, S., Nakanishi, T., Takamatsu, S., Tomita, K., 1997. Visualization of pH Change of E. coli with a Novel pH Imaging Microscope. Bioimages 5(4), 143-147.

Yoshinobu, T., Iwasaki, H., Ui, Y., Furuichi, K., Ermolenko, Y., Mourzina, Y., Wagner, T., Näther, N., Schöning, M.J., 2005. The light-addressable potentiometric sensor for multi-ion sensing and imaging. Methods 37(1), 94-102.

Yoshinobu, T., Miyamoto, K.-i., Werner, C.F., Poghossian, A., Wagner, T., Schöning, M.J., 2017. Light-Addressable Potentiometric Sensors for Quantitative Spatial Imaging of Chemical Species. Annu. Rev. Anal. Chem. 10(1), 225-246.

Zandi, O., Schon, A.R., Hajibabaei, H., Hamann, T.W., 2016. Enhanced Charge Separation and Collection in High-Performance Electrodeposited Hematite Films. Chem. Mater. 28(3), 765-771.

Zarei, L., Tavallaie, R., Choudhury, M.H., Parker, S.G., Bakthavathsalam, P., Ciampi, S., Gonçales, V.R., Gooding, J.J., 2018. DNA-Hybridization Detection on Si(100) Surfaces Using Light-Activated Electrochemistry: A Comparative Study between Bovine Serum Albumin and Hexaethylene Glycol as Antifouling Layers. Langmuir 34(49), 14817-14824.

Zhang, D.W., Wu, F., Krause, S., 2017. LAPS and SPIM Imaging Using ITO-Coated Glass as the Substrate Material. Anal. Chem. 89(15), 8129-8133.

Zhou, B., Das, A., Kappers, M.J., Oliver, R.A., Humphreys, C.J., Krause, S.J.S., 2019. InGaN as a Substrate for AC Photoelectrochemical Imaging. Sensors 19(20), 4386.

Graphical abstract